


Article

UV and Visible Light Induced Photodegradation of Reactive Red 198 Dye and Textile Factory Wastewater on Fe₂O₃/Bentonite/TiO₂ Nanocomposite

Shakiba Mohammadhosseini ¹, Tariq J. Al-Musawi ², Rosario Mireya Romero Parra ³, Mutaz Qutob ⁴, M. Abdulfadhil Gatea ⁵, Fatemeh Ganji ⁶ and Davoud Balarak ^{7,*} 

¹ Department of Environmental Health Engineering, Mazandaran University of Medical Sciences, Mazandaran 4815733971, Iran

² Building and Construction Techniques Engineering Department, Al-Mustaqbal University College, Hillah 51001, Iraq

³ Department of General Studies, Continental University, Lima 15304, Peru

⁴ Department of Civil Engineering, Faculty of Engineering, Isra University, Amman 11622, Jordan

⁵ Technical Engineering Department College of Technical Engineering, The Islamic University, Najaf 54001, Iraq

⁶ Student Research Committee, Zahedan University of Medical Sciences, Zahedan 9816743463, Iran

⁷ Department of Environmental Health, Health Promotion Research Center, Zahedan University of Medical Sciences, Zahedan 9816743463, Iran

* Correspondence: dbalarak2@gmail.com



Citation: Mohammadhosseini, S.; Al-Musawi, T.J.; Romero Parra, R.M.; Qutob, M.; Gatea, M.A.; Ganji, F.; Balarak, D. UV and Visible Light Induced Photodegradation of Reactive Red 198 Dye and Textile Factory Wastewater on Fe₂O₃/Bentonite/TiO₂ Nanocomposite. *Minerals* **2022**, *12*, 1417. <https://doi.org/10.3390/min12111417>

Academic Editor: Luciana Sciascia

Received: 16 September 2022

Accepted: 5 November 2022

Published: 8 November 2022

Publisher's Note: MDPI stays neutral with regard to jurisdictional claims in published maps and institutional affiliations.



Copyright: © 2022 by the authors. Licensee MDPI, Basel, Switzerland. This article is an open access article distributed under the terms and conditions of the Creative Commons Attribution (CC BY) license (<https://creativecommons.org/licenses/by/4.0/>).

Abstract: In the present study, the objective was to probe the capacity of the Fe₂O₃/Bentonite/TiO₂ (Fe₂O₃/B/TiO₂) nanoparticles to act as a catalyst in degrading the reactive red 198 (RR198) dye and textile factory wastewater, utilizing irradiation with visible and UV light. The efficiency of this degradation was studied for a variety of experimental parameters by employing real samples of textile wastewater. After 60 min of reaction time, complete degradation of the target pollutant was visible using the synthesized catalyst, i.e., Fe₂O₃/B/TiO₂, under UV light; the same effect was noted after 90 min under visible light. Further, the ease of separation and quick collection of the synthesized Fe₂O₃/B/TiO₂ can result in keeping the photocatalytic efficiency high, as well as raising the reusability. The photocatalytic processes under UV and visible light were found capable of converting the non-biodegradable textile wastewater into biodegradable one. Besides, with the introduction of *Daphnia magna*, the toxicity of the effluent was examined. Through photocatalysis, utilizing both techniques, the dye toxicity in the solution was fully neutralized, and the intensity of toxicity of the textile effluent was lowered by around 70%. The conclusion drawn in this study showed that the synthesized catalyst displayed good efficiency in removing organic compounds from the textile effluents by both photocatalytic processes using UV and visible light.

Keywords: textile wastewater; degradation; reactive red 198 dye; Fe₂O₃/B/TiO₂ catalyst; photocatalytic process

1. Introduction

The rapid growth in the global population, coupled with the alarming reduction in drinking water resources, has become a grave concern in terms of the drinking water supply requirements of several countries worldwide [1,2]. Water scarcity, observed at a global level, has intensified due to the escalation in environmental pollution and made the supply of sanitary water for the populace one of the foremost issues today [3,4]. The wastewater released by the textile industry processes often contains a large variety of dyes and chemicals [5,6]. Most of the dyes employed in this industry are non-biodegradable because they form strong complexes [7,8]. Under anaerobic conditions, a few of the dyes decompose and release carcinogenic aromatic amines into the effluent, posing a hazard to the health of humans and animals [9]. The reactive and acid dyes, among the various

dyes, present the greatest issues, which is why their removal becomes crucial [10,11]. Dyes are regarded as toxic substances and are capable of causing harmful effects, inducing skin allergies, skin irritation, and mutations. On the other hand, synthetic dyes exert their effect on photosynthetic activity, thus affecting the viability of aquatic life by producing a barrier that blocks sunlight from reaching them [12]. Also, some dyes which contain aromatic compounds and various metals in their structure cause toxicity, imposing a high hazard to the life of the aquatic ecosystems [13–15]. Therefore, it becomes crucial and necessary to identify efficient and modern methods for removing these compounds from the various kinds of effluents [16,17].

As conventional biological treatment techniques are either incapable of degrading the dyes or have very poor efficiency, many other methods are used, such as advanced oxidation, photocatalytic oxidation, membrane separation, Ozonation, and ultrasonic dyeing [18]. However, all these processes include intrinsic limitations, including poor rates of degradation, reduced mineralization, expensive operating costs, inflexible operating conditions, and so forth [19]. Hence, in the past few years, more advanced oxidation processes have been employed as relevant alternatives to conventional treatment techniques as they are easy to use, economically cost-effective, and very efficient. These methods involve exposing the contaminants to UV radiation using nanoparticles as the photocatalyst. The contaminants are oxidized and undergo photodegradation by developing hydroxyl radicals [20]. The extent of the photocatalytic degradation of the pollutants is dependent on some parameters, i.e., the pH, initial concentration of the contaminant, and light intensity [21].

Titanium dioxide (TiO_2) and zinc oxide are the most prominent of the various photocatalysts. At present, the most popular one is TiO_2 or titania, as it is non-toxic, cheap, easily available, and chemically and biologically stable [22]. The crystal structure, shape, and particle size of titania are a strong influence on its application and performance. Although titania comes in three crystalline forms, rutile, anatase, and brookite, the anatase phase shows the highest stability at temperatures under $711\text{ }^\circ\text{C}$ and is highly photocatalytic [23]. During the application of suspended nanoparticles, the TiO_2 nanoparticles, in particular, produce one problem, which is their separation from the aqueous medium after the process and recycling. This is overcome by magnetizing the nanoparticles, such as using Fe_2O_3 nanoparticles. However, magnetization does not solve the formation of aggregation and agglomeration of the nanoparticles [24]. The nanoparticles stabilized on the supporting material can raise their stability by averting aggregation and agglomeration. To stabilize the nanoparticles on a solid substrate, many methods have been employed for electrodeposition, sol-gel, chemical vapor deposition, thermal treatment, hydrothermal, and cation exchange reaction. Of these, nanoparticle synthesis is performed by the molten salt technique, a new, cheap and quick method avoiding the need for costly equipment and tools [25]. Several varieties of stabilization substrates were also tested, such as glass beads, glass tubes, glass wool, quartz, anti-corrosion steel, aluminum, activated carbon, and silica. Bentonite, among these bases, is a fine-grained clay made up of swelling minerals (mostly Montmorillonite and a little beidellite). Due to its strong ability for adsorption, intense porosity, and good capacity for cation exchange, as well as low price, bentonite offers many advantages [26].

The degradability of the dye through photocatalysis under UV radiation was examined by Isari et al. (2018) using a TiO_2 photocatalyst; in this process, 100% dye removal was achieved at a pH of 7 after 150 min [27]. In their work, Khan et al. (2019) employed the TiO_2 /Graphene oxide technique for 200 min and completely degraded methylene blue dye, using 30 mg/mL as the initial concentration [28]. The method cited above included one disadvantage where the suspended TiO_2 nanophotocatalyst was used. This made it difficult for the nanoparticles to separate from the solution. Due to their very minute size, the separation was incomplete, with some materials remaining in the solution. Also, the time involved in the complete degradation of the dye was too long, resulting in raising the costs for energy consumption by several times [29].

In this study, the degradation of reactive red 198 dye and real wastewater has been done, which has not been done in most of the degradation studies with real textile wastewater. Also, in this study, reaction kinetics was investigated. The amount of energy consumed by different catalysts has been compared in terms of cost with different studies. Effluent toxicity was also done with *Daphnia magna*. All the specifications of the catalyst were done completely. Finally, the mechanism of destruction through scavengers was discussed. Therefore, this study is very comprehensive compared to similar studies, and all the required parameters have been discussed, which has been done in a few studies.

On reviewing the literature and scrutinizing previous investigations, it was confirmed that no research had been reported thus far on the removal of reactive red 198 (RR198) dye from aqueous solutions using the combined three materials of $\text{Fe}_2\text{O}_3 + \text{Bentonite} + \text{TiO}_2$ (named here: $\text{Fe}_2\text{O}_3/\text{B}/\text{TiO}_2$). Therefore, the main objective of the current study was to synthesize $\text{Fe}_2\text{O}_3/\text{B}/\text{TiO}_2$ and use it as a separable photocatalyst to degrade the RR198 dye at different conditions. Using the new-molten salt method, the synthesis of nanoparticles was performed. No equipment, except a furnace, was required for this technique. Investigation of the physical properties of the magnetized nanoparticles was done with the help of XRD, TEM, XPS, SEM, DRS, FTIR, VSM, BET, and XRF. Also, during the operation of this process, in the present study, the optimal parameters desired were studied using real textile wastewater. The toxicity of the effluent was tested before and after the treatment using *Daphnia magna*. By performing the BOD_5/COD analyses, the biodegradability of the wastewater of the effluent was ascertained, and the energy consumed was finally calculated.

2. Material and Methods

2.1. Chemicals and Reagents

Titanium dioxide (rutile nano-powder, particle size < 100 nm, 99.5%, CAS Number: 1317-80-2) was procured from Sigma Aldrich. For the current work, the hydrochloric acid, sodium hydroxide, and $\text{FeCl}_3 \cdot 6\text{H}_2\text{O}$ were prepared by Merck Company. The RR198 dye (Molecular Formula of $\text{C}_{27}\text{H}_{18}\text{ClN}_7\text{Na}_4\text{O}_{16}\text{S}_5$, CAS Number = 145017-98-7 and Molecular Weight = 968.2 g/mol) was purchased from the Alvan Sabet Factory. First, the initial solution of the RR198 dye was prepared at 1000 mg/L, and the solutions needed for the present study were composed using distilled water to dilute the initial solution. It is noteworthy that all the samples were prepared with deionized water (Milli-Q Academic-Millipore).

2.2. Synthesis Steps and Characterization Analysis

To synthesize the bentonite supported on TiO_2 [29], the Molten salt method was adopted. Here, 10 g of bentonite and 10 g of TiO_2 powder were placed in a porcelain mortar and ground together. This mixture was then put in an oven at 500 °C for 60 min. Next, this sample was removed from the oven, washed three times using distilled water, and finally filtered. The solution was maintained at room temperature for 24 h and subjected to 12 h of drying at 80 °C to produce aerogels.

The first step in the preparation of bentonite-supported Fe_2O_3 -doped TiO_2 ($\text{Fe}_2\text{O}_3/\text{B}/\text{TiO}_2$) was the addition of 40 g of $\text{FeCl}_3 \cdot 6\text{H}_2\text{O}$ to 50 mL of distilled water. Next, to this solution, 10 g of the xerogel prepared in the prior step was added. This was then homogenized by placing it on a shaker for 2 h. Next, it was transferred to the oven at 70 °C for 4 h, after which a brown precipitate was formed. Then, calcination of this precipitate was done at 600 °C in an N_2 atmosphere. Finally, these calcined samples were drawn and subjected to three washes with deionized water and then immediately oven-dried for 2 h.

Several methods to characterize the $\text{Fe}_2\text{O}_3/\text{B}/\text{TiO}_2$ were adopted using the surface charge, FTIR (Fourier Transform Infra-Red Spectrophotometry), SEM (MIRA III-TESCAN FESEM), and XRD (XRD; PW1730, Philips). Employing x-ray fluorescence spectroscopy (SGS Geosol Laboratorios Ltda, Brazil), the chemical composition was derived. The pH_{pzc} (or the pH at which the adsorbent carries no charge) or the isoelectric points of the bentonite was 5.3, and that of the $\text{Fe}_2\text{O}_3/\text{B}/\text{TiO}_2$ was 6.2. With the help of a vibrating sample magnetometer (VSM; LAKESHORE-7304), the magnetic properties were determined. By

analyzing the N_2 adsorption-desorption isotherm and BJH utilizing a Micromeritics Analyzer (ASAP 2460) at 77 K, the surface area and pore size were estimated. Besides, the pH value of the $Fe_2O_3/B/TiO_2$ for the point of zero charge (pH_{pzc}) analysis was ascertained.

2.3. Photocatalytic Experiments

All the experiments were conducted in the batch system on a laboratory scale. In the present work, the reactor selected had a volume of 500 mL. For the photocatalytic process, the UV-C lamp (15 W, Philips G8 T5) and visible light (40 W, Hg vapor lamp) were used together with the $Fe_2O_3/B/TiO_2$ synthesized in the prior step as the catalyst. The addition of 300 mL of the desired dye was done to the reactor at every step of the experiment. First, the pH of the solution was adjusted, and the solution was then placed in a quartz chamber, after which it was transferred to a beaker so that the surface of the solution inside the beaker was fully raised to receive maximum exposure to the light. A distance of 2.5 cm was maintained between the lamps and the surface of the solution in the reactor. To avert any evaporation of the sample due to exposure to the heat generated by the lamps, a continuous flow of water was kept in circulation. Once the sample was placed inside the reactor with the $Fe_2O_3/B/TiO_2$ acting as the catalyst, the pH was adjusted to the desired value, the lamps were lighted, and the process was started. A magnetic stirrer was used to mix the contents of the reactor. Samples were drawn from the reactor surface at the specific times of 10, 20, 30, 40, 50, 60, 90, and 120 min via a pipette and poured into a 10 mL beaker. To achieve photocatalytic separation, isolation of the sample was done using a 0.45-micron Whatman filter and magnet. The dye concentration in each sample was assessed using a Hach spectrophotometer, model DR-5000, at a maximum wavelength of 280 nm. The pH was adjusted using 0.1 N HCl and 0.1 N NaOH.

Employing the open reflux method, the COD values were estimated. In short, this method involved the oxidation of the organic matter with potassium dichromate in an acidic condition. The quantity of BOD_5 was established by determining the oxygen consumed via titration with sodium thiosulfate, post-incubation (of 5 days).

To study the rate of recycling the photocatalyst and reusing it, the experiments to degrade the dye, RR198, included six consecutive stages. When the test period was completed, the nanocomposite used was filtered after centrifugation. This was rinsed several times with distilled water and reused as a photocatalyst. Finally, using *Daphnia Magna*, the bioassay method was employed for the toxicity test. The use of *Daphnia* provided a significant advantage because of its parthenogenesis, which raised the validity of the findings. The *Daphnia*, harvested from fish stocks, was transferred to an aquarium containing the culture medium, having both a thermometer and an aerator.

3. Results and Discussion

3.1. Characteristics of $Fe_2O_3/B/TiO_2$ Catalyst

In this study, the FTIR analysis was performed for TiO_2 , Bentonite, and $Fe_2O_3/B/TiO_2$ (Figure 1a) from 400 to 4000 $1/cm$. The absorption peaks for $Fe_2O_3/B/TiO_2$ were observed at 3438, 1629, 1091, 1043, 932, and 539 $1/cm$. The ones detected at 3442, 3438, and 1629 $1/cm$ were understood to be caused by the stretching vibration and bending vibration of the OH; this occurred because the water adsorbed onto the surfaces of the samples. The high adsorption at 1040 $1/cm$ is ascribed to the asymmetric stretching of the Si-O-Si bonds belonging to the SiO_2 as the main component of bentonite; this indicates the successful loading of catalysts onto the bentonite. The absorption band noted at 400–600 $1/cm$ is connected to the stretching vibration of the Ti-O bond [29]. The adsorption peak seen at 932 $1/cm$ is attributed to the Ti-O-Si produced during the calcination process. Finally, the peak at 539 $1/cm$ is attributed to the Fe-O, which suggests that the doping of the catalyst with Fe has been effective (i.e., the Fe atom has been substituted successfully with Ti).

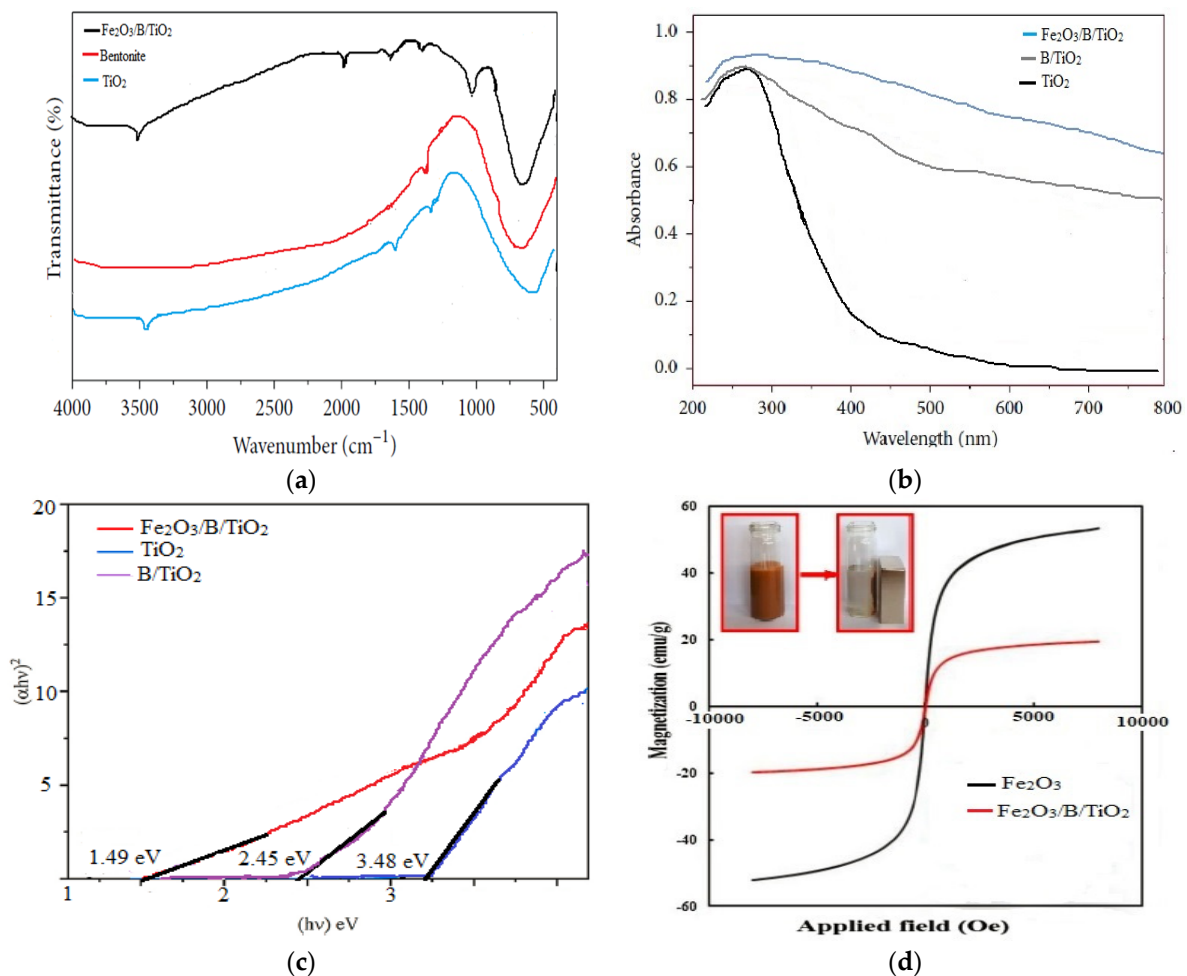


Figure 1. FTIR spectra of bentonite, TiO_2 , and $\text{Fe}_2\text{O}_3/\text{B}/\text{TiO}_2$ (a), Diffuse reflectance UV-Vis spectra (b), Tauc plot derived from the Kubelka Munk Function for band gap energy (c), Magnetic hysteresis curves (d).

Typically, during the naturally occurring photodegradation processes, the photocatalyst absorbs the ultraviolet (UV) and visible light from natural sunlight and uses its energy for the reactions involved in the redox degradation. Using the UV/Vis diffuse reflectance spectra, the absorption of the UV and visible light of the photocatalyst was done to characterize the TiO_2 , B/TiO_2 , and $\text{Fe}_2\text{O}_3/\text{B}/\text{TiO}_2$ composites (Figure 1b). From Figure 1b, it is easy to detect significant absorption of light by the TiO_2 at wavelengths less than 390 nm, the intrinsic absorption edge of TiO_2 for transferring the electron from the $\text{O}2\text{p}$ to the $\text{Ti}3\text{d}$, and which corresponds to the valence band, to the conduction band transition of the TiO_2 . For the TiO_2 , in the absence of Fe and bentonite doping, practically no light absorption was observed in the region of visible light (400 to 800 nm). As the capacity of the bentonite to absorb visible light is good, greater absorption of visible light is expected by the B/TiO_2 when compared to the bare TiO_2 . In fact, Figure 1b reveals that, by doping the TiO_2 with Fe^{3+} and bentonite, the absorption of visible light can be substantially improved by forming a dopant energy level within the band gap of the TiO_2 caused by the Fe^{3+} doping or Fe_2O_3 . As verified from the documents available, the Fe_2O_3 , which possesses a narrow band gap ($E_g = 2.1$ eV), can absorb and utilize around 70% ($\text{Fe}_2\text{O}_3/\text{B}/\text{TiO}_2$) of the incident solar spectra. As evident in Figure 1b, it is possible to obtain the band gap (E_g) by the Kubelka–Munk function (Equation (1)). From the results of the calculations (Figure 1c), the TiO_2 , B/TiO_2 , and $\text{Fe}_2\text{O}_3/\text{B}/\text{TiO}_2$ revealed band gaps of 3.48, 2.45, and 1.49 eV, respectively; as is observed, the smallest band gap was related to the $\text{Fe}_2\text{O}_3/\text{B}/\text{TiO}_2$

and it was easy to excite its electrons from the valence band to the conduction band when exposed to irradiation from visible light [30]:

$$(\alpha \times hv)^2 = B(hv - E_g) \quad (1)$$

where α is the optical absorption coefficient (1/cm), $h\nu$ is the photon energy (eV), E_g is the bandgap value (eV), and B is a constant ($=1 \text{ eV/cm}^2$).

The vibrating sample magnetometer revealed the residual magnetic loops of the catalysts (Figure 1d). The saturation magnetization (M_s) values of 57.3 and 17.2 emu/g were noted for Fe_2O_3 and $\text{Fe}_2\text{O}_3/\text{B}/\text{TiO}_2$, respectively. In Figure 1d, the ferromagnetic behavior with coercivity (H_c) was found to be around 63 Oe for the Fe_2O_3 nanoparticles; also, superparamagnetic behavior with H_c near zero was ascertained for $\text{Fe}_2\text{O}_3/\text{B}/\text{TiO}_2$. Of note, the supermagnetic property of $\text{Fe}_2\text{O}_3/\text{B}/\text{TiO}_2$ can enable this catalyst to separate from the solution through an external magnetic field.

The morphologies and microstructures of the $\text{Fe}_2\text{O}_3/\text{B}/\text{TiO}_2$ were observed by SEM and TEM. The images from the FESEM analysis can be seen in Figure 2a,b. In the FESEM image of bentonite (Figure 2a), the particles are visible as spherical and transparent. From the image of $\text{Fe}_2\text{O}_3/\text{B}/\text{TiO}_2$ (Figure 2b), the particles appear as aggregates clogging the bed's surface.

Figure 2c demonstrated that the TiO_2 nanoparticles in $\text{Fe}_2\text{O}_3/\text{TiO}_2$ were aggregated, and the particle size of TiO_2 was about 15 nm. However, the size of TiO_2 in $\text{Fe}_2\text{O}_3/\text{B}/\text{TiO}_2$ was about 11 nm (Figure 2d). That was because the particle size of anatase TiO_2 is smaller than rutile TiO_2 . Figure 2c,d showed that the TiO_2 nanoparticles were attached to the bentonite, which means that the bentonite prevents the aggregation of TiO_2 nanoparticles.

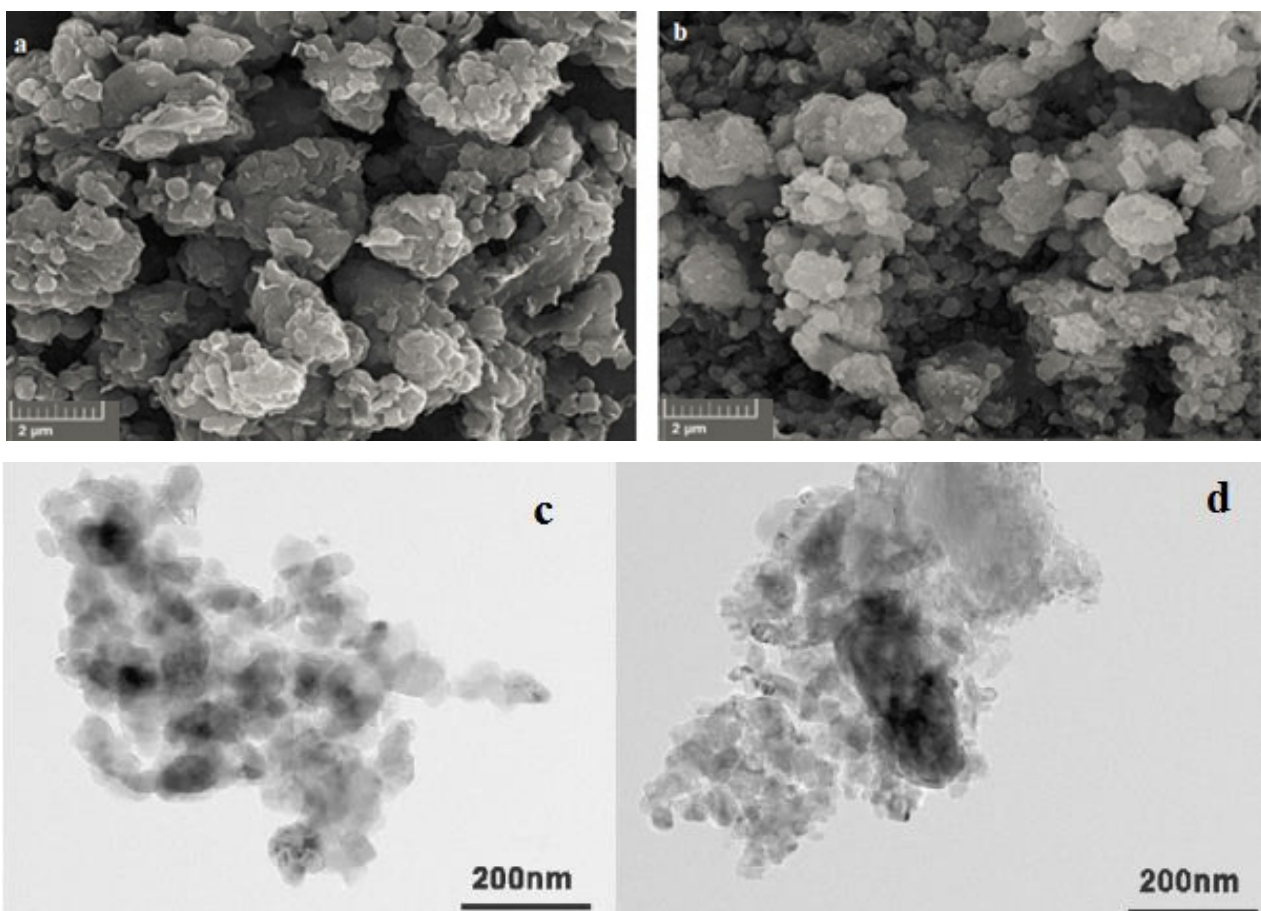


Figure 2. Cont.

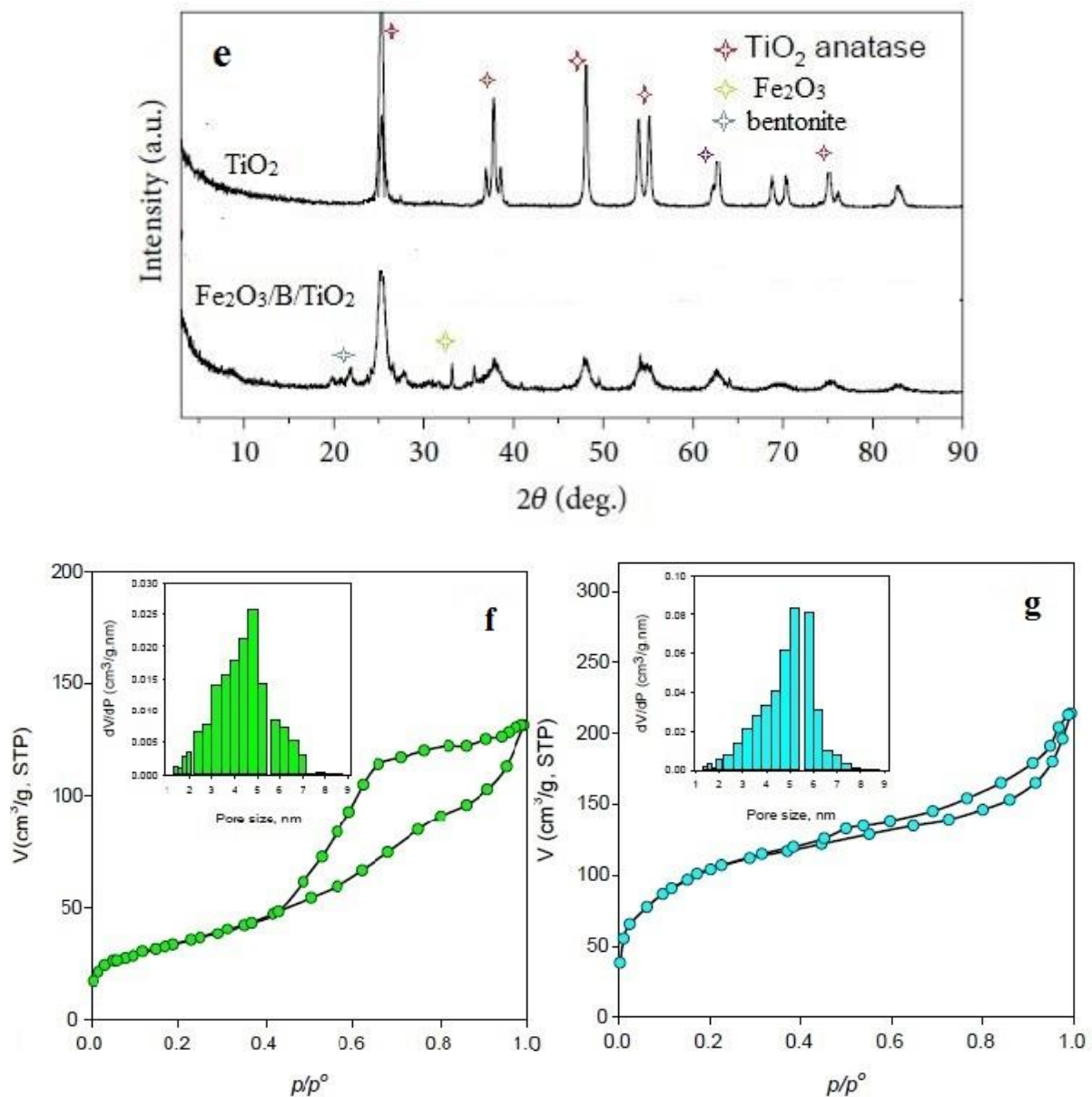


Figure 2. SEM images of bentonite (a), SEM images of Fe₂O₃/B/TiO₂ (b), TEM images of Fe₂O₃/TiO₂ and Fe₂O₃/B/TiO₂ (c,d), XRD patterns of Fe₂O₃/B/TiO₂ (e), N₂ adsorption-desorption isotherms Inset: distributions of pore size from the adsorption branches using the BJH method N₂ adsorption-desorption isotherm (f,g).

Using the XRD analysis, the crystalline structures of TiO₂ and Fe₂O₃/B/TiO₂ were assessed. From the results given in Figure 2e, the diffraction peaks visible at 2θ of 27.6°, 36.4°, 41.2°, and 54.3° correlated with the rutile TiO₂. A variety of diffraction peaks at 2θ values of 25.2°, 38.7°, 48.1°, 53.9°, and 55.2° were noted for the Fe₂O₃/B/TiO₂, and ascribed to the (101), (112), (200), (105), and (211) planes of the anatase TiO₂, respectively. The XRD patterns showed that the rutile phase was produced in pure TiO₂ at 600 °C, the calcination temperature. However, in Fe₂O₃/B/TiO₂, the anatase was seen in the crystallization phase of the TiO₂. Further, at about 2θ of 22.4°, a few small peaks were identified, which included peaks of the diffraction angles of bentonite [30]. Besides, from the calculation using the Scherrer formula, the average sizes of the TiO₂ and Fe₂O₃/B/TiO₂ particles were approximately 22.1 nm and 7.2 nm, respectively, which indicates that the TiO₂ growth can be impeded through Fe doping and bentonite loading.

The results of the nitrogen sorption isotherms acknowledged for bentonite, and $\text{Fe}_2\text{O}_3/\text{B}/\text{TiO}_2$ composites are shown in Figure 2f,g. In Figure 2f, which is linked to the adsorption isotherm of bentonite, the presence of some quantity of micropores in the structure of this material is suggested. The solids possessing some microporous structure (type I) have type I adsorption isotherm profile with the capacity for rapid uptake of nitrogen gas by the solid at relative pressure, which is rather low (p/p°), and accepted as the characteristic of such types of solids. As the relative pressure increases, the isotherm is transformed to type II, with the presence of a large hysteresis loop, as revealed in Figure 4a. This hysteresis loop is considered the H2-type hysteresis. The pore volume and BET surface area for bentonite are found to be $0.317 \text{ cm}^3/\text{g}$ and $86.9 \text{ m}^2/\text{g}$, respectively.

As displayed in Figure 2g, the TiO_2 and Fe_2O_3 added to the bentonite resulted in altering the type of the sorption isotherms of the composites from type I/II to type IV, with an H3-H4 hysteresis loop, implying that non-rigid aggregates of plate-like particles are present, showing the contribution of the micropores and mesopores in the $\text{Fe}_2\text{O}_3/\text{B}/\text{TiO}_2$. While the BET surface area of the $\text{Fe}_2\text{O}_3/\text{B}/\text{TiO}_2$ composite is $194.2 \text{ m}^2/\text{g}$, the total pore volume is $0.251 \text{ cm}^3/\text{g}$. Further, the pore size distribution (PSD) of bentonite and composites was determined by the Density Functional Theory (DFT) having medium regularization. The results of this are shown in Figure 2f,g (as insert graphics). From this Figure, all of the solids can be seen to have mostly mesoporous structures.

XPS analysis was employed to investigate the surface and chemical states of $\text{Fe}_2\text{O}_3/\text{B}/\text{TiO}_2$. As shown in Figure 3a, the $\text{Fe}_2\text{O}_3/\text{B}/\text{TiO}_2$ sample was composed of five elements: Fe, O, Ti, Si, and Al. The C1s peak was attributed to the adventitious hydrocarbon from the XPS instrument. The high-resolution XPS spectra of Ti, Fe, and Si are shown in Figure 3b–d. The Ti 2p XPS spectrum was observed at 459.1 eV and 465.2 eV, corresponding to the binding energy peaks of Ti 2p_{3/2} and Ti 2p_{1/2}, respectively (Figure 3b). These binding energies were assigned to Ti^{4+} from TiO_2 . In Figure 3c, the binding energies of Fe 2p_{3/2} and Fe 2p_{1/2} were located at 709.8 eV and 724.5 eV, respectively. The satellite peak was observed at around 717.8 eV. Mentioned peaks were attributed to Fe^{3+} from Fe_2O_3 . The Si 2p XPS spectrum was observed at 102.9 eV (Figure 3d), corresponding to SiO_2 , which was the main component of bentonite. The XPS result further demonstrated that the $\text{Fe}_2\text{O}_3/\text{B}/\text{TiO}_2$ composites were synthesized successfully.

As evident from Table 1, a little quantity of Fe_2O_3 was seen in raw bentonite, which achieved 20.4% in the fabricated catalyst. Also, the quantity of TiO_2 in the catalyst touched 11.6%, and when these two compounds are present in the catalyst, it indicates that the desired catalyst was synthesized.

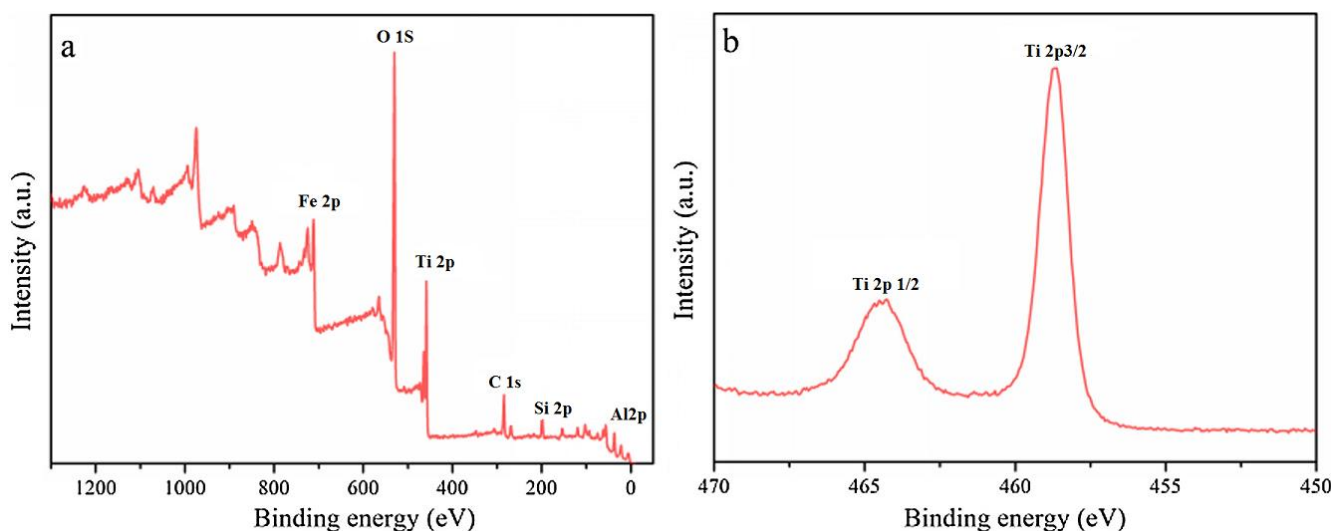


Figure 3. Cont.

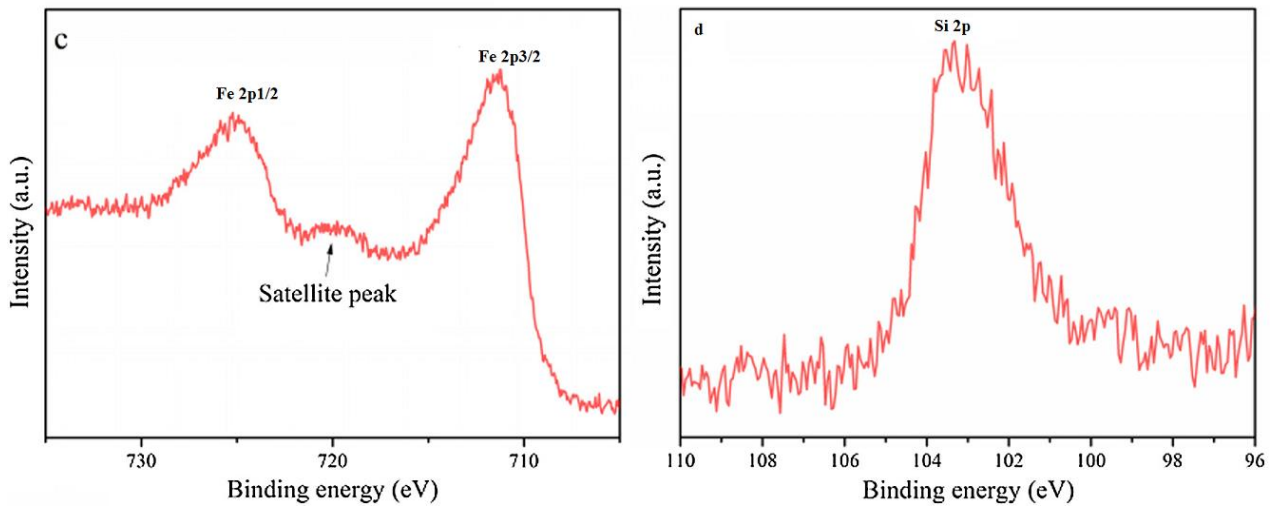


Figure 3. XPS spectra of catalysts: (a) Survey spectrum, (b) Ti 2p spectrum, (c) Fe 2p spectrum, (d) Si 2p spectrum.

Table 1. Chemical composition of the samples of bentonite and Fe₂O₃/B/TiO₂ (mass %).

Material	Al ₂ O ₃	SiO ₂	Fe ₂ O ₃	TiO ₂	Na ₂ O	MgO	CaO	MnO	K ₂ O
Bentonite	24.4	59.9	2.65	—	1.73	4.55	2.64	0.86	2.75
Fe ₂ O ₃ /B/TiO ₂	20.7	34.7	20.4	11.6	1.65	4.39	2.6	0.85	2.7

3.2. Comparison of RR198 Degradation by Two Methods Using UV Lamp and Visible Light

By comparing the photocatalytic efficiency, a careful study of the degradation of RR198 was done with the addition of 0.6 g/L of a variety of catalyst composites (B/TiO₂, TiO₂, and Fe₂O₃/B/TiO₂). The RR198 removal percentage was assessed after the reaction under UV irradiation (Figure 4a) and visible light (Figure 4b) for several time intervals. The highest photocatalytic activity for RR198 degradation (100% removal) was observed under UV light irradiation for 60 min and linked to the Fe₂O₃/B/TiO₂. The photocatalytic degradation efficiencies of RR198 by TiO₂ and B/TiO₂ after 60 min were 65.2% and 77.6%, respectively. Further, when visible light was used, the fastest degradation of RR198 was also accomplished through the use of Fe₂O₃/B/TiO₂, resulting in 100% removal of the dye in 90 min. Besides, 22.7 and 59.2% of RR198 were degraded with the help of TiO₂ and B/TiO₂, respectively. As cited earlier, the Fe₂O₃/B/TiO₂ facilitated the achievement of the fastest rate of the degradation of RR198 under both UV and visible lights; this is attributed to possibly the highest specific surface area and most UV-Vis adsorption observed for the Fe₂O₃/B/TiO₂ [31].

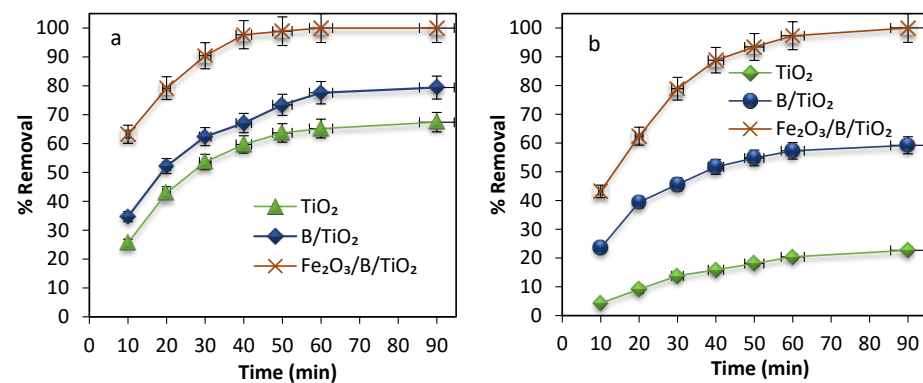


Figure 4. Cont.

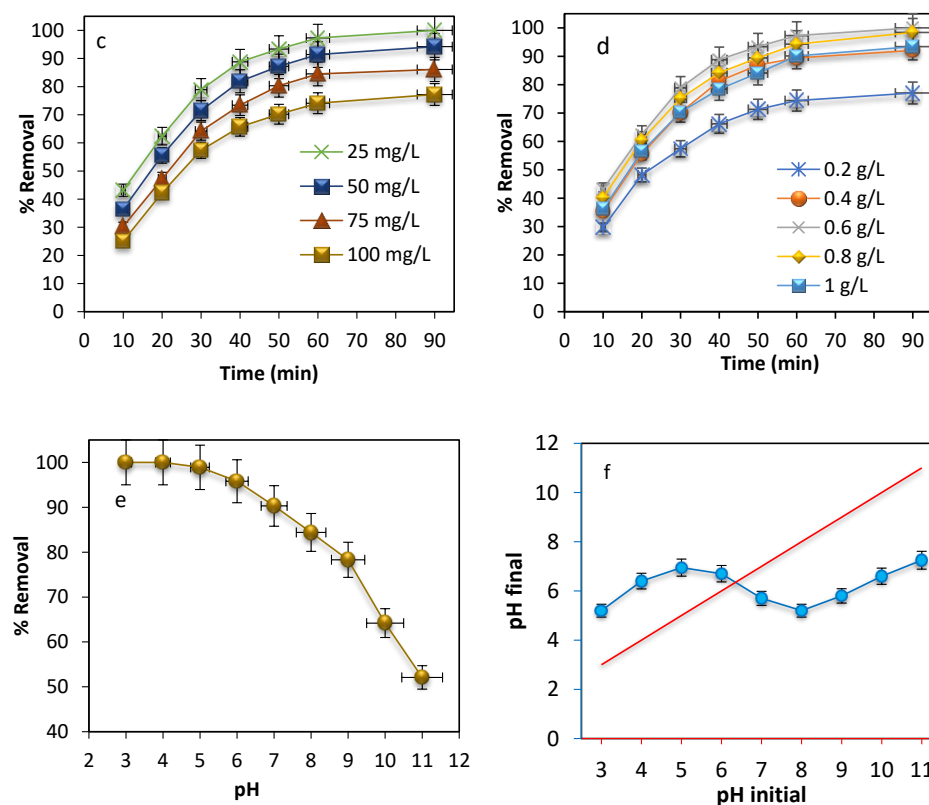


Figure 4. Comparison of RR198 degradation by UV light (a), Comparison of RR198 degradation by Visible light (b), Effects of RR198 concentration (c), Effects of Fe₂O₃/B/TiO₂ dosage (d), Effects of solution pH (e), Determination of the pH_{pzc} (f).

3.3. Effect of Different Parameters on RR198 Dye Degradation by Visible Light

Employing a variety of initial RR198 concentrations ($C_0 = 10, 25, 50,$ and 100 mg/L) was a good way to investigate the effect exerted by the initial RR198 concentration on the rate of photodegradation. In fact, from Figure 4c, the rate of RR198 degradation was observed to reduce through a rise in the dye concentration. As the initial concentration of the RR198 increased gradually, more dye molecules got attached to the photocatalyst surface, thus covering the active sites of the Fe₂O₃/B/TiO₂ and reaching a fewer number of photons on the surface of the photocatalyst; this caused the formation of lesser numbers of •OH radicals and fewer •OH ones that could attack the dye molecules [32].

One of the crucial parameters in the process of photocatalytic degradation is the dosage of the photocatalyst. Hence, the optimal photocatalyst dosage was determined through the use of a variety of quantities of the Fe₂O₃/B/TiO₂ composite (0.1–1.0 g/L). From Figure 4d, it is obvious that as the doses of the photocatalyst increased in the range of 0.1 to 0.6 g/L, it was possible to detect an increase in the RR198 degradation. A description of the event cited is provided based on supplying greater amounts of the photocatalyst, which result in more activated centers and, therefore, the adsorption of more reactant [33]. However, when higher photocatalyst loading (from 0.6 to 1.0 g/L) was performed, a drop was noted in the percentage of the RR198 degradation. Any rise in the turbidity of the mixtures caused a decline in the amount of light transmitted through the solution, as well as a blockage of the light penetration on all the surface particles available, which was the reason for the cited event [34]. In light of the results (Figure 3d), i.e., achieving the maximum percentage of degradation (100%) for 0.5 g of photocatalyst dosage, it was selected for use in studies done later.

Notably, pH is one of the main factors which influences the action of the photocatalyst in an aqueous medium; this index markedly alters the particle surface load, redox potential, and position of the energy bands. In fact, Uzunova-Bujnova et al. [34] highlighted

that the influence exerted by the pH has a bearing on the potential characteristics of the photocatalytic surface and can be explained based on the Point of Zero Charge (pH_{pzc}). In this study, the removal achieves the highest percentage at a pH of 3 and then decreases as the pH increases (Figure 4e).

For the $Fe_2O_3/B/TiO_2$ particles, the zero-point potential is 6.4. When the pH is less than 6.4 (Figure 4f) or is indicative of acidic pH, the catalyst surface gets positively charged, which therefore causes anionic compounds such as the RR198 dye to be adsorbed by the photocatalyst and the cationic compounds to be rejected. On the other hand, at pH values that exceed 6.4, the catalyst surface gets negatively charged, resulting in the adsorption of cationic compounds and the repulsion of the anions [35]. In their study, Zhu et al. [36] focused on methyl orange dye and found that the highest level of decolorization occurred at 97% of dye removal at a pH of 2; this was ascribed to the electrostatic attraction between the positive surface of the catalyst and the methyl orange dye anions. Typically, it can be stated that because the RR198 is also an anionic dye, it gets better adsorbed onto the photocatalytic particles that carry a positive charge when the pH is acidic. The removal process shows higher efficacy and is more effective when the pH is acidic than when it is alkaline.

3.4. Stability and Reusability of the Photocatalyst

To keep the conditions optimal, the reusability of the $Fe_2O_3/B/TiO_2$ photocatalyst was tested for the degradation of RR198. From Figure 5a, no significant decrease was observed in the removal efficiency after the photocatalyst was used four times. In the present work conducted for dye removal, the photocatalyst cited above was isolated and used in the next step. From Figure 5a, it is clear the synthetic photocatalyst has a high dye removal efficiency for reuse up to 8 times, and only a 10% reduction was noted. It may also be the cause for the RR198 to penetrate the internal pores of the catalyst that is found in the active sites; superficial washing does not free the active sites [37].

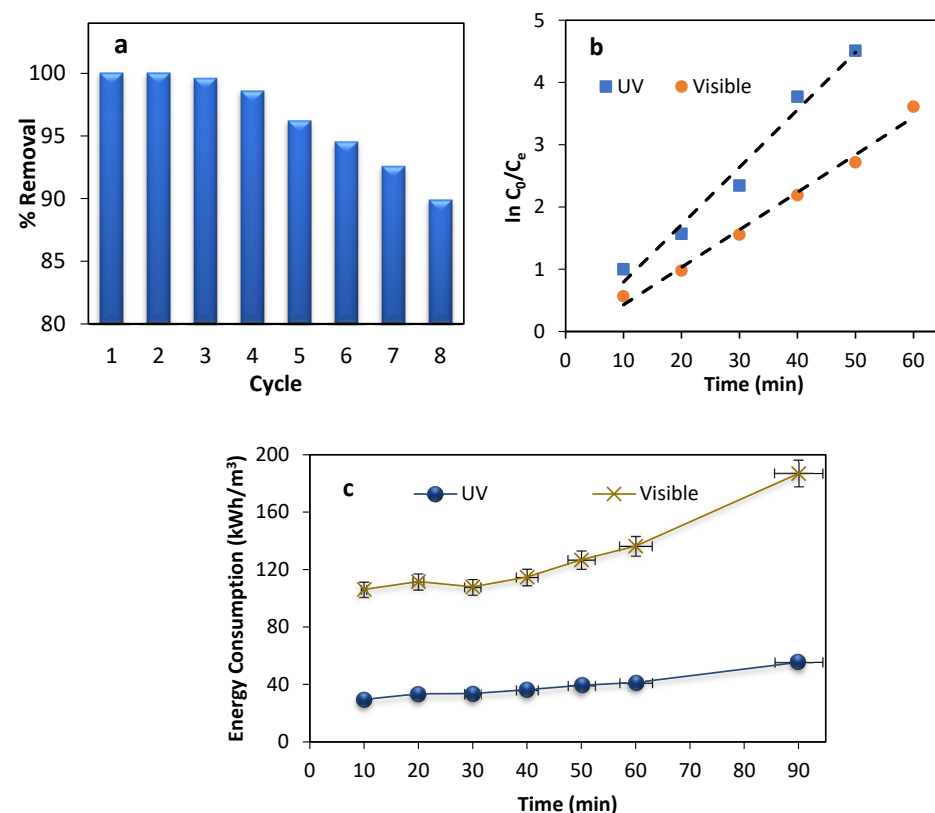


Figure 5. Results from the experiment to determine reusability (a), Pseudo-first-order kinetics (b), Energy consumed by both processes (c).

3.5. Reaction Kinetics

The photocatalytic reaction kinetics of the organic compounds can be expressed by the Pseudo First Order (PFO) or Hinshelwood-Langmuir model. This model is linked to the degradation rate and concentration of organic compounds, expressed in Equation (2) [38]:

$$r = \frac{dC}{dt} = \frac{K_d k_r C}{1 + KC} \quad (2)$$

where k_r is the main constant rate (1/min), and K_d = absorption equilibrium constant (1/mg).

When there is relatively low adsorption or low concentration of the organic compound, Equation (2) can be made simpler or expressed as first-order kinetics, with a known constant rate (K , 1/min) (Equation (3)):

$$\ln \frac{C_0}{C_e} = Kt \quad (3)$$

where C_0 and C_e represent the RR198 dye concentrations (mg/L) at the initial and after a specific time (t , minutes) of the photocatalytic reaction, respectively.

Based on the PFO model and evident from Figure 5b, the data of $\ln \frac{C_0}{C_e}$ is plotted against the reaction time, seen as a straight line, while the slope of the graph reveals the rate constant (k). Based on this, the degradation of the RR198 by photocatalysis in both models of destruction goes according to the PFO kinetics. Further, the reaction rate constant was seen to be equal to 0.092 1/min for the RR198 degradation when visible light was used and 0.06 1/min when UV light was used; this indicates that under UV light, the rate of reaction of destruction is 1.5 times faster than when visible light is utilized.

3.6. Determining Energy Consumption

In recent years, the quantity of energy consumed and the expenditure involved in wastewater treatment (per m^3 of treated wastewater) is among the significant problems connected with treatment methods and comparing the different methods. The energy consumption (EC) in kWh/m^3 during the photocatalytic process under UV and visible light was estimated using the following Equation [39]:

$$EC = \frac{P \times t \times 1000}{V \times 60 \times \log\left(\frac{C_0}{C_e}\right)} \quad (4)$$

In this equation, V refers to the volume of the dye solution within the photochemical reactor; t signifies the time taken to treat the dye solution containing the RR198, and P implies the input power (kW) of the treatment system.

For both methods, the energy consumption results at different times are revealed in Figure 5c. The energy consumption during the 10 to 60 min of destruction under UV light is equal to 29.6 to 55.3 kWh/m^3 . Also, for the same time duration, for color degradation under visible light from a lamp, the EC was found to be 106.2 to 186.8 kWh/m^3 . In their work, Lin et al. [40] reported that during the removal of phenol by the photocatalytic process using TiO_2 as the particle catalyst, the energy consumed was reported to rise as the contact time increased. The energy consumed for removing 80% of phenol in 90 min was found to be 145.5 kWh/m^3 . Further, Kumar et al. [41] reported that removing the Acid Black 1 dye by ZnO nanoparticles showed energy consumption equal to 121.2 kWh/m^3 . Comparing the results reported with these studies, it is evident that the $Fe_2O_3/B/TiO_2$ catalyst utilizes less energy under UV light than other nanocomposites.

3.7. Effluent Toxicity Test

Among the most crucial parameters to assess the efficiency of the treated effluent is effluent toxicity [42]. In this work, toxicity was tested with a bioassay using *Daphnia Magna* (DM). For the test, the DM neonates (younger than 24 h) were collected with a plastic pipette and subjected to three washes with water. They were then placed in an

exposure chamber where the dye was present. Next, a series of glasses were chosen, one of which was regarded as the control, in which the dye concentration was zero. All the glasses used were new and subjected to washing in 1% nitric acid. Then, 10 DM was added to each glass. Next, in the laboratory glasses, 10, 20, 40, 50, 75, 100, and 100 mg/L of the dye were prepared and observed after 24, 48, 72, and 96 h. When the test was completed, the number of live neonates was counted. To confirm, every test was repeated. At 24 and 48 h, their immobility or mortality was estimated, and neonates that could not swim in 15 s after gentle shaking were regarded as dead. The Lethal concentration 50 (LC50) values for 24, 48, 72, and 96 h were found to be 45.2, 31.4, 22.3, and 11.9 mg/L, respectively. In the control solution containing the culture medium, the survival rate of the DM was 100%, but in the 50 mg/L solution of RR198, post 24 h, the survival rate of the DM was zero. After photocatalysis, employing UV and Visible light, 100% of the DM in the effluent survived. It shows the total decrease in effluent toxicity caused by the solution containing the RR198 dye. A review of the study was also done with textile industry wastewater before and after the photocatalytic process. The initial wastewater from the textile industry had high toxicity, and 100% of the DMs were destroyed during the beginning few hours of exposure, implying the high toxicity of the wastewater and high sensitivity of the DM. However, the photocatalytic process utilizing both methods, with the UV and visible lamps, caused a significant decrease in the toxicity of the treated samples. In this context, a 70% reduction in toxicity was observed with both methods.

3.8. Experiments with Textile Factory Wastewater

The wastewater in this study was prepared from the inlet of the treatment plant of a textile factory and transported in dark-colored containers to the laboratory. Testing of the samples was done in the laboratory at 20 °C. The COD of the wastewater was 3200 mg/L, while the BOD₅ was 620 mg/L, and the BOD₅/COD ratio was 0.19, suggesting the non-biodegradability of the textile wastewater. The electrical conductivity was 1820 µS/cm, while the soluble solids were 1120 mg/L, at normal pH of 6.1. Both UV and visible light were used for the test. The optimal conditions maintained in the earlier steps, such as 90 min of contact time and 0.6 g/L doses of catalyst, were adopted in this test as well. In Figure 6, the results are shown, where the removal rate was 87.1% under UV light, and in the final effluent, the BOD₅/COD ratio achieved was 0.61; however, for the experiments under visible light, the removal rate of the COD touched 83.6%, and in the final effluent, the BOD₅/COD was 0.55. Of note, any wastewater having a BOD₅/COD ratio below 0.4 is categorized as non-biodegradable [43–45]. As both methods converted the non-biodegradable textile wastewater into biodegradable wastewater, it is suggested that they be utilized to treat the wastewater emanating from textile factories before the biological treatment.

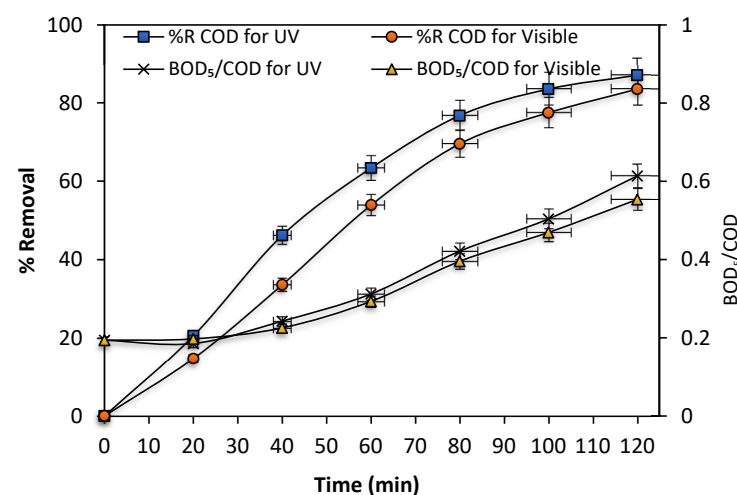


Figure 6. Elimination of COD in real textile wastewater and degradability of the final effluent.

3.9. Scavenger Test

In general, the reactive species accountable for the photocatalytic oxidative reaction in the aqueous phase are as listed: hydroxyl radicals ($\bullet\text{OH}$), superoxide radicals ($\bullet\text{O}_2^-$), photogenerated holes (h^+ VB), and electrons (e^- CB). For performing the scavenging experiments, isopropyl alcohol (IPA, 0.1 mg/L), benzoquinone (BZQ, 0.1 mg/L), ammonium oxalate (AO, 0.1 mg/L), and Cr(VI) (0.1 mg/L) ion were used as the $\bullet\text{OH}$, $\bullet\text{O}_2^-$, h^+ VB, and e^- CB scavengers, respectively [46,47]. From Figure 7, the effect the scavengers exert on the photocatalytic efficiency of $\text{Fe}_2\text{O}_3/\text{B}/\text{TiO}_2$ is evident. When AO, IPA, BZQ, and Cr(VI) were added, the removal efficiencies detected were 76.2, 46.1, 81.4, and 82.5%, respectively. Compared to other scavengers (AO, IPA), a slight effect was also observed in the Cr(VI) and BZQ. In the scavenging experiments, the $\bullet\text{OH}$ species were recognized as the principal oxidizing species in the degradation process, and they substantially lowered the photocatalytic activity [48].

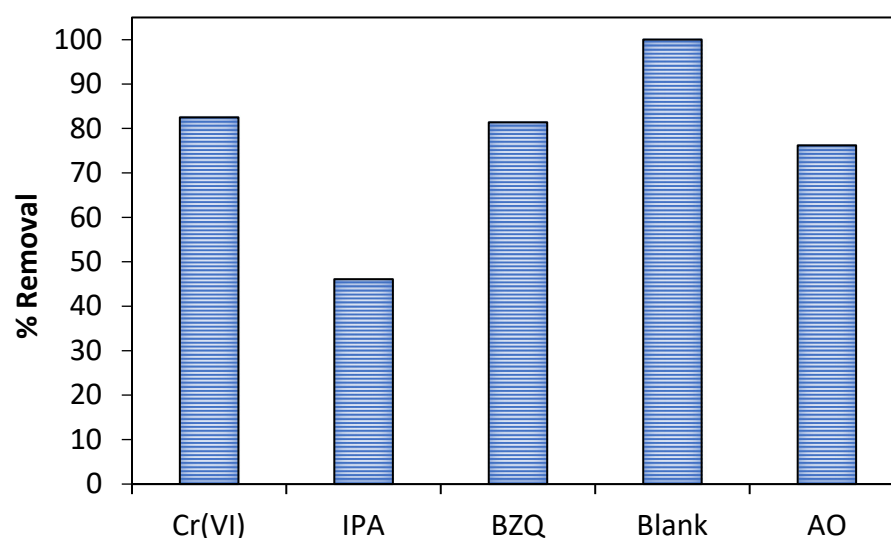


Figure 7. Photocatalytic degradation of RR198 over $\text{Fe}_2\text{O}_3/\text{B}/\text{TiO}_2$ in the presence of scavengers.

3.10. Elucidation of the Mechanism

Based on the outcomes of the experiments described in Figure 7, a reaction mechanism was proposed for the degradation of RR198. The RR198 adsorbed was first activated by visible light; during this photo-activation process, electron transfer occurred from the RR198 (RR198^*) in the singlet excited state to the CB of $\text{Fe}_2\text{O}_3/\text{B}/\text{TiO}_2$, leaving the h^+ in the VB [49]. Following this step, the reaction between the electrons in the CB and O_2 resulted in the generation of the $\bullet\text{O}_2^-$ and $\bullet\text{OH}$ radicals, according to process I, as Figure 1 reveals. Nevertheless, depending upon the results of the trapping experiment, the indirect effect of the $\bullet\text{O}_2^-$ on the RR198 degradation (caused by the $\bullet\text{OH}$ production) cannot be neglected; however, this process is not the main degradation mechanism [50].

The $\bullet\text{O}_2^-$ may participate solely in a side reaction or perhaps produce more $\bullet\text{OH}$ for the degradation. At the same time, the h^+ in the VB can take part in the oxidization of the OH^- released by the ionization of water to the $\bullet\text{OH}$ (the main active free radical for RR198 degradation), as shown in process III (Figure 8) [51].

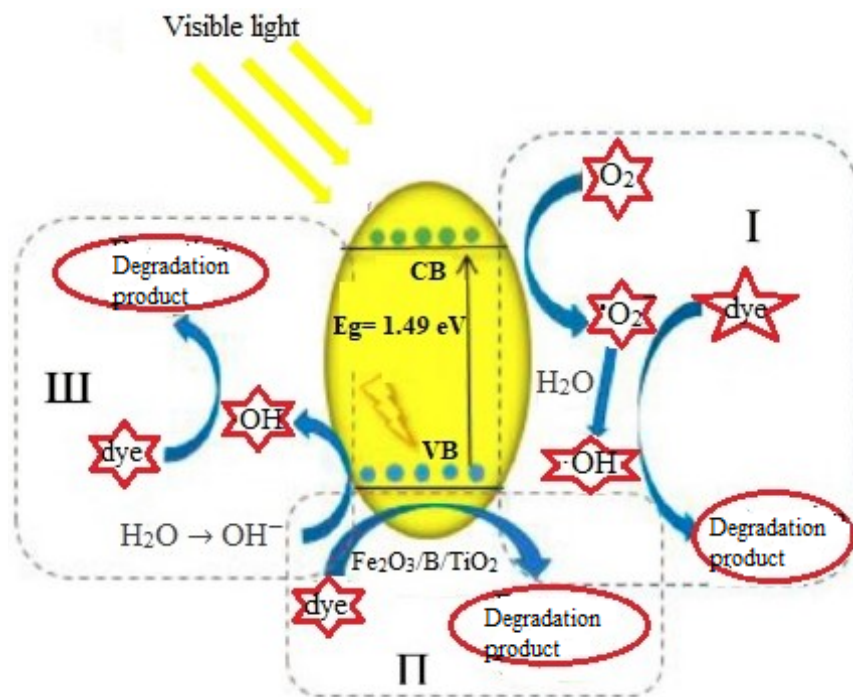
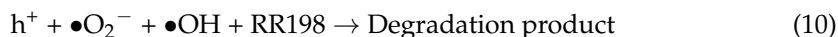
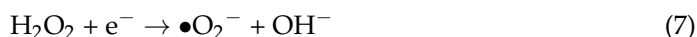
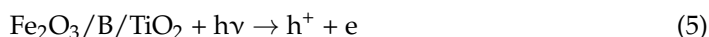


Figure 8. Mechanism of RR198 degradation via photocatalysis with Fe₂O₃/B/TiO₂.

In due course, the •O₂[−] and •OH degrade the RR198⁺ and RR198, reflective of the main part played by the •OH in the degradation system. Simultaneously, the h⁺ directly degrades the RR198⁺ and RR198 (which can be deduced from the results of the trapping experiment), as revealed in process II (Figure 7). Nonetheless, through this process, a minor percentage of the RR198 was degraded [52]. Thus, the conclusion drawn that the processes present in the degradation system are process III (the main mechanism), process II (which occurs very infrequently), and process I requires further study based on the result of the present experiment. The reactions listed are linked to complete sequences [53,54]:



4. Conclusions

The current work investigated the effective parameters in the advanced oxidation process used in the degradation of the RR198 dye, employing the Fe₂O₃/B/TiO₂ nanocomposite, and determined the optimal conditions for its removal. A comparative study was done on the photocatalytic process using both visible and ultraviolet radiation. From Tauc’s graph, the band gap value for TiO₂ dropped from 3.48 eV to 1.49 eV for the Fe₂O₃/B/TiO₂ nanocomposite. Therefore, the Fe₂O₃/B/TiO₂ catalysts synthesized revealed notable photocatalytic activity in the AB113 degradation under visible light when compared to the TiO₂ and B/TiO₂ catalysts. The maximum efficiency (100%) of the photocatalytic process under UV light was accomplished when the dye concentration was 25 mg/L, at a pH of 3, and a 0.6 g/L dose of Fe₂O₃/B/TiO₂ after 50 min. Under similar conditions and employing visible light, a 94.2% removal rate was observed, with total removal achieved after 90 min. Further, the photocatalyst, even after 8 reuses, continues to remain stable and

removes the dye, thus confirming the economics of the photocatalysis. As both processes have successfully converted the non-biodegradable textile wastewater into biodegradable wastewater, it is possible to suggest that these techniques be used in wastewater treatment from textile factories before the biological process. Using DM, the final effluent was checked for toxicity, where all the DMs were alive in the colored solution effluent, thus indicating a total fall in the toxic levels of the effluent. Also, the final textile effluent revealed a 70% decrease in toxicity.

Author Contributions: Conceptualization, S.M.; methodology, T.J.A.-M. and R.M.R.P.; formal analysis, M.Q.; data curation, F.G.; writing—original draft preparation, D.B. and M.A.G. All authors have read and agreed to the published version of the manuscript.

Funding: This paper is funded by Zahedan University of Medical Sciences, Zahedan, Iran (code project; 10816).

Data Availability Statement: Not applicable.

Acknowledgments: The authors express their thankfulness to the Student Research Committee of Zahedan University of Medical Sciences for the financial support provided. Also, the authors wish to acknowledge the Al-Mustaqbal University College (Babylon, Iraq).

Conflicts of Interest: The authors declare no conflict of interest.

References

1. Balarak, D.; Al-Musawi, T.J.; Mohammed, I.A.; Abasizadeh, H. The eradication of reactive black 5 dye liquid wastes using *Azolla filiculoides* aquatic fern as a good and an economical biosorption agent. *SN Appl. Sci.* **2020**, *2*, 1015. [\[CrossRef\]](#)
2. Ruan, S.; Huang, W.; Zhao, M.; Song, H.; Gao, Z. A Z-scheme mechanism of the novel ZnO/CuO nn heterojunction for photocatalytic degradation of Acid Orange 7. *Mater. Sci. Semicond. Process.* **2020**, *107*, 104835. [\[CrossRef\]](#)
3. Liu, X.; Yuan, B.; Zou, J.; Wu, L.; Dai, L.; Ma, H.; Li, K.; Ma, J. Cu (II)-enhanced degradation of acid orange 7 by Fe (II)-activated persulfate with hydroxylamine over a wide pH range. *Chemosphere* **2020**, *238*, 124533. [\[CrossRef\]](#) [\[PubMed\]](#)
4. Sillanpää, M.; Mahvi, A.H.; Balarak, D.; Khatibi, A.D. Adsorption of Acid orange 7 dyes from aqueous solution using Polypyrrole/nanosilica composite: Experimental and modelling. *Int. J. Environ. Anal. Chem.* **2021**, *101*, 1–11.
5. Jose, M.; Aswathi, P.; Sriram, K.; Parakh, P.; Prakash, H. Ion-exchange bonded H₂Ti₃O₇ nanosheets-based magnetic nanocomposite for dye removal via adsorption and its regeneration via synergistic activation of persulfate. *RSC Adv.* **2016**, *6*, 80133–80144. [\[CrossRef\]](#)
6. Dhanasekar, M.; Ratha, S.; Rout, C.S.; Bhat, S.V. Efficient sono-photocatalytic degradation of methylene blue using nickel molybdate nanosheets under diffused sunlight. *J. Environ. Chem. Eng.* **2017**, *5*, 2997–3004. [\[CrossRef\]](#)
7. May-Lozano, M.; Mendoza-Escamilla, V.; Rojas-García, E.; López-Medina, R.; Romero, G.R.; Martínez-Delgado, S.A. Sonophotocatalytic degradation of Orange II dye using low cost photocatalyst. *J. Clean. Prod.* **2017**, *148*, 836–844. [\[CrossRef\]](#)
8. Balarak, D.; Mostafapour, F.K.; Joghataei, A. Adsorption of Acid Blue 225 dye by Multi Walled Carbon Nanotubes: Determination of equilibrium and kinetics parameters. *Pharm. Chem.* **2016**, *8*, 138–145.
9. Ghanbari, F.; Zirrahi, F.; Lin, K.; Kakavandi, B.; Hassani, A. Enhanced electro-peroxone using ultrasound irradiation for the degradation of organic compounds: A comparative study. *J. Environ. Chem. Eng.* **2020**, *5*, 104167. [\[CrossRef\]](#)
10. Wang, C.Q.; Jiang, X.Y.; Huang, R.; Cao, Y.J.; Xu, J.; Han, Y.F. Copper/carbon composites from waste printed circuit boards as catalysts for Fenton-like degradation of Acid Orange 7 enhanced by ultrasound. *AIChE J.* **2019**, *65*, 1234–1244. [\[CrossRef\]](#)
11. Ramos, D.; González, M.V.; Muñoz, R.; Cruz, J.S.D. Obtaining and Characterization of TiO₂-GO Composites for Photocatalytic Applications. *Int. J. Photoenergy* **2020**, *2020*, 3489218. [\[CrossRef\]](#)
12. Martins, P.M.; Ferreira, C.G.; Silva, A.R.; Magalhães, B. TiO₂/graphene and TiO₂/graphene oxide nanocomposites for photocatalytic applications: A computer modeling and experimental study. *Compos. Part B* **2018**, *145*, 39–46. [\[CrossRef\]](#)
13. Basturk, E.; Işık, M.; Karatas, M. Removal of aniline (Methylene Blue) and azo (Reactive Red 198) dyes by photocatalysis via nano TiO₂. *Desalin Water Treat.* **2019**, *143*, 306–313.
14. Hasanzadeh, M.; Jorfi, S.; Ahmadi, M.; Jaafarzadeh, N. Hybrid Sono-photocatalytic degradation of Acid Brown 14 Using Persulphate and ZnO Nanoparticles: Feasibility and kinetic Study. *Int. J. Environ. Anal. Chem.* **2020**, *100*, 1–14. [\[CrossRef\]](#)
15. Akpan, U.G.; Hameed, B.H. Parameters affecting the photocatalytic degradation of dyes using TiO₂-based photocatalysts: A review. *J. Hazard. Mater.* **2009**, *170*, 520–529. [\[CrossRef\]](#)
16. Kumar, R.; Kumar, G.; Akhtar, M.; Umar, A. Sonophotocatalytic degradation of methyl orange using ZnO nano-aggregates. *J. Alloys Compd.* **2015**, *629*, 167–172.
17. Reza, K.M.; Kurny, A.; Gulshan, F. Parameters affecting the photocatalytic degradation of dyes using TiO₂: A review. *Appl Water Sci.* **2017**, *7*, 1569–1578. [\[CrossRef\]](#)

18. Elmolla, E.S.; Chaudhuri, M. Degradation of amoxicillin, ampicillin and cloxacillin antibiotics in aqueous solution by the UV/ZnO photocatalytic process. *J. Hazard. Mater.* **2010**, *173*, 445–449. [[CrossRef](#)]
19. Saleh, T.A.; Gondal, M.; Drmash, Q.; Yamani, Z.; Al-Yamani, A. Enhancement in photocatalytic activity for acetaldehyde removal by embedding ZnO nano particles on multiwall carbon nanotubes. *Chem. Eng. J.* **2011**, *166*, 407–412. [[CrossRef](#)]
20. Khan, M.A.N.; Siddique, M.; Wahid, F.; Khan, R. Removal of reactive blue 19 dye by sono, photo and sonophotocatalytic oxidation using visible light. *Ultrason. Sonochem.* **2015**, *26*, 370–377. [[CrossRef](#)]
21. Khataee, A.; Karimi, A.; Zarei, M.; Joo, S.W. Eu-doped ZnO nanoparticles: Sonochemical synthesis, characterization, and sonocatalytic application. *Ultrason. Sonochem.* **2020**, *67*, 102822. [[PubMed](#)]
22. Kakavandi, B.; Bahari, N.; Kalantary, R.R. Enhanced sono-photocatalysis of tetracycline antibiotic using TiO₂ decorated on magnetic activated carbon (MAC@T) coupled with US and UV: A new hybrid system. *Ultrason. Sonochem.* **2019**, *55*, 75–85. [[PubMed](#)]
23. Mirzaei, A.; Yerushalmi, L.; Chen, Z.; Haghighat, F.; Guo, J. Enhanced photocatalytic degradation of sulfamethoxazole by zinc oxide photocatalyst in the presence of fluoride ions: Optimization of parameters and toxicological evaluation. *Water Res.* **2018**, *132*, 241–251. [[PubMed](#)]
24. Houas, A.; Lachheb, H.; Ksibi, M.; Elaloui, E.; Guillard, C.; Herrmann, J.-M. Photocatalytic degradation pathway of methylene blue in water. *Appl. Catal. B* **2001**, *31*, 145–157. [[CrossRef](#)]
25. Eshaq, G.; Wang, S.; Sun, H.; Sillanpaa, M. Superior performance of FeVO₄@CeO₂ uniform core-shell nanostructures in heterogeneous Fenton-sonophotocatalytic degradation of 4-nitrophenol. *J. Hazard. Mater.* **2020**, *382*, 121059. [[CrossRef](#)]
26. Azarpira, H.; Sadani, M.; Abtahi, M.; Vaezi, N.; Rezaei, S.Z. Photo-catalytic degradation of triclosan with UV/iodide/ZnO process: Performance, kinetic, degradation pathway, energy consumption and toxicology. *J. Photochem. Photobiol. A* **2019**, *371*, 423–432. [[CrossRef](#)]
27. Isari, A.A.; Payan, A.; Fattahi, M.; Jorfi, S.; Kakavandi, B. Photocatalytic degradation of rhodamine B and real textile wastewater using Fe-doped TiO₂ anchored on reduced graphene oxide (Fe-TiO₂/rGO): Characterization and feasibility, mechanism and pathway studies. *Appl. Surf. Sci.* **2018**, *62*, 549–564. [[CrossRef](#)]
28. Khan, S.A.; Arshad, Z.; Shahid, S.; Arshad, I.; Rizwan, K. Synthesis of TiO₂/Graphene oxide nanocomposites for their enhanced photocatalytic activity against methylene blue dye and ciprofloxacin. *Compos. Part B* **2019**, *175*, 107120. [[CrossRef](#)]
29. Ahmad, S.; Yasin, A. Photocatalytic degradation of deltamethrin by using Cu/TiO₂/bentonite composite. *Arab. J. Chem.* **2020**, *13*, 8481–8488. [[CrossRef](#)]
30. Szczepanik, B. Photocatalytic degradation of organic contaminants over clay TiO₂ nano composites: A review. *Appl. Clay Sci.* **2017**, *141*, 227–239. [[CrossRef](#)]
31. Silvestri, S.; Foletto, E.L. Preparation and characterization of Fe₂O₃/TiO₂/clay plates and their use as photocatalysts. *Ceram. Int.* **2017**, *43*, 4057–4062. [[CrossRef](#)]
32. Devi, L.G.; Kavitha, R. A review on non metal ion doped titania for the photocatalytic degradation of organic pollutants under UV/solar light: Role of photogenerated charge carrier dynamics in enhancing the activity. *Appl. Catal. B Environ.* **2013**, *140–141*, 559–587. [[CrossRef](#)]
33. Ghorai, T.K.; Chakraborty, M.; Pramanik, P. Photocatalytic performance of nanophotocatalyst from TiO₂ and Fe₂O₃ by mechanochemical synthesis. *J. Alloys Compd.* **2011**, *509*, 8158–8164.
34. Uzunova-Bujnova, M.; Kralchevska, R.; Milanova, M.; Todorovska, R.; Hristov, D. Todorovsky, Crystal structure, morphology and photocatalytic activity of modified TiO₂ and of spray-deposited TiO₂ films. *Catal. Today* **2010**, *151*, 14–20. [[CrossRef](#)]
35. Ziylan-Yavas, A.; Mizukoshi, Y.; Maeda, Y.; Ince, N.H. Supporting of pristine TiO₂ with noble metals to enhance the oxidation and mineralization of paracetamol by sonolysis and sonophotolysis. *Appl. Catal. A* **2015**, *172*, 7–17.
36. Zhu, H.; Jiang, R.; Fu, Y.; Guan, Y.; Xiao, L.; Yao, J. Effective photocatalytic decolorization of methyl orange utilizing TiO₂/ZnO/chitosan nanocomposite films under simulated solar irradiation. *Desalination* **2012**, *286*, 41–48. [[CrossRef](#)]
37. Kamranifar, M.; Al-Musawi, T.J.; Amarzadeh, M.; Qutob, M.; Arghavan, F.S. Quick adsorption followed by lengthy photodegradation using FeNi₃@SiO₂@ZnO: A promising method for complete removal of penicillin G from wastewater. *J. Water Process Eng.* **2021**, *40*, 101940.
38. Rajiv, P.; Mengelizadeh, N.; McKay, G.; Balarak, D. Photocatalytic degradation of ciprofloxacin with Fe₂O₃ nanoparticles loaded on graphitic carbon nitride: Mineralisation, degradation mechanism and toxicity assessment. *Int. J. Environ. Anal. Chem.* **2021**, *101*, 1–15. [[CrossRef](#)]
39. Arghavan, F.S.; Al-Musawi, T.J.; Allahyari, E.; Nasseh, N.; Hossein Panahi, A. Complete degradation of tamoxifen using FeNi₃@SiO₂@ZnO as a photocatalyst with UV light irradiation: A study on the degradation process and sensitivity analysis using ANN tool. *Mater. Sci. Semicond. Process.* **2021**, *128*, 105725. [[CrossRef](#)]
40. Lin, S.H.; Chiou, C.H.; Chang, C.K.; Juang, R.S. Photocatalytic degradation of phenol on different phases of TiO₂ particles in aqueous suspensions under UV irradiation. *J. Environ. Manag.* **2011**, *92*, 3098–3104. [[CrossRef](#)]
41. Krishna Kumar, B.; Selvam, K.; Velmurugan, R.; Swaminathan, M. Influence of operational parameters on photomineralization of Acid Black 1 with ZnO. *Desalin Water Treat.* **2010**, *24*, 132–139. [[CrossRef](#)]
42. Sarafraz, M.; Amini, M.M.; Adiban, M.; Eslami, A. Facile synthesis of mesoporous black N-TiO₂ photocatalyst for efficient charge separation and the visible-driven photocatalytic mechanism of ibuprofen degradation. *Mater. Sci. Semicond. Process.* **2020**, *120*, 105258.

43. Farzadkia, M.; Bazrafshan, E.; Esrafil, A.; Yang, J.-K.; Shirzad-Siboni, M. Photocatalytic degradation of Metronidazole with illuminated TiO₂ nanoparticles. *J. Environ. Health Sci. Eng.* **2015**, *13*, 35. [[CrossRef](#)] [[PubMed](#)]
44. Al-Musawi, T.J.; Mengelizadeh, N.; Taghavi, M.; Shehu, Z. Capability of copper-nickel ferrite nanoparticles loaded onto multi-walled carbon nanotubes to degrade acid blue 113 dye in the sonophotocatalytic treatment process. *Environ. Sci. Pollut. Res.* **2022**, *29*, 51703–51716. [[CrossRef](#)]
45. Liu, X.; Li, W.; Hu, R.; Wei, Y. Synergistic degradation of acid orange 7 dye by using non-thermal plasma and g-C₃N₄/TiO₂: Performance, degradation pathways and catalytic mechanism. *Chemosphere* **2020**, *249*, 126093. [[CrossRef](#)]
46. Masoud, M.; Nourbakhsh, A.; Hassanzadeh-Tabrizi, S.A. Influence of modified CNT-Ag nanocomposite addition on photocatalytic degradation of methyl orange by mesoporous TiO₂. *Inorg. Nano-Met. Chem.* **2017**, *47*, 1168–1174. [[CrossRef](#)]
47. Bhavani, R.; Sivasamy, A. Sonocatalytic degradation of malachite green oxalate by a semiconductor metal oxide nanocatalyst. *Ecotoxicol. Environ. Saf.* **2016**, *134*, 403–411.
48. Isari, A.A.; Mehregan, M.S.; Hayati, F.; Kalantary, R.R. Sono-photocatalytic degradation of tetracycline and pharmaceutical wastewater using WO₃/CNT heterojunction nanocomposite under US and visible light irradiations: A novel hybrid system. *J. Hazard. Mater.* **2020**, *390*, 122050. [[CrossRef](#)]
49. Khataee, A.; Rad, T.S.; Nikzat, S.A.; Hassani, M.H. Fabrication of NiFe layered double hydroxide/reduced graphene oxide (NiFe-LDH/rGO) nanocomposite with enhanced sonophotocatalytic activity for the degradation of moxifloxacin. *Chem. Eng. J.* **2019**, *375*, 122102. [[CrossRef](#)]
50. Al-Musawi, T.J.; Mengelizadeh, N.; Sathishkumar, K.; Mohebi, S. Preparation of CuFe₂O₄/montmorillonite nanocomposite and explaining its performance in the sonophotocatalytic degradation process for ciprofloxacin. *Colloid Interface Sci. Commun.* **2021**, *45*, 100532.
51. Balarak, D.; Rajiv, P.; Chandrika, K. Photocatalytic degradation of amoxicillin from aqueous solutions by titanium dioxide nanoparticles loaded on graphene oxide. *Environ. Sci. Pollut. Res.* **2021**, *28*, 49743–49754. [[CrossRef](#)] [[PubMed](#)]
52. Yilmaz, M.; Mengelizadeh, N.; Saloot, M.K.; Shahbaksh, S. Facile synthesis of Fe₃O₄/ZnO/GO photocatalysts for decolorization of acid blue 113 under solar, visible and UV lights. *Mater. Sci. Semicond. Process.* **2022**, *144*, 106593. [[CrossRef](#)]
53. Al-Musawi, T.J.; Rajiv, P.; Mengelizadeh, N.; Sadat Arghavan, F. Photocatalytic efficiency of CuNiFe₂O₄ nanoparticles loaded on multi-walled carbon nanotubes as a novel photocatalyst for ampicillin degradation. *J. Mol. Liq.* **2021**, *337*, 116470. [[CrossRef](#)]
54. Dianati, R.A.; Mengelizadeh, N.; Zazouli, M.A. Photocatalytic degradation of bisphenol A by GO-TiO₂ nanocomposite under ultraviolet light: Synthesis, effect of parameters and mineralisation. *Int. J. Environ. Anal. Chem.* **2022**. [[CrossRef](#)]